Atomistic Insight into Ion Transport and Conductivity in Ga/Al-Substituted $Li_7La_3Zr_2O_{12}$ Solid Electrolytes

Fabián A. García Daza,*,† Mauricio R. Bonilla,† Anna Llordés,‡,¶ Javier Carrasco,*,‡ and Elena Akhmatskaya†,¶

†*BCAM - Basque Center for Applied Mathematics, Alameda de Mazarredo 14, E-48009 Bilbao, Spain*

‡*CIC EnergiGUNE, Albert Einstein 48, E-01510 Miñano, Spain*

¶*IKERBASQUE, Basque Foundation for Science, María Díaz de Haro 3, E-48013 Bilbao, Spain*

E-mail: fgarcia@bcamath.org; jcarrasco@cicenergigune.com

Abstract

Garnet-structured $Li_7La_3Zr_2O_{12}$ is a promising solid electrolyte for next-generation solid-state Li batteries. However, sufficiently fast Li-ion mobility required for battery applications only emerges at high temperatures, upon a phase transition to cubic structure. A well-known strategy to stabilize the cubic phase at room temperature relies on aliovalent substitution; in particular, the substitution of Li^+ by Al^{3+} and Ga^{3+} ions. Yet, despite having the same formal charge, Ga^{3+} substitution yields higher conductivities (10^{-3} S/cm) than Al^{3+} (10^{-4} S/cm). The reason of such difference in ionic conductivity remains a mystery. Here we use molecular dynamic simulations and advanced sampling techniques to precisely unveil the atomistic origin of this phenomenon.

Our results show that Li^+ vacancies generated by Al^{3+} and Ga^{3+} substitution remain adjacent to Ga^{3+} and Al^{3+} ions, without contributing to the promotion of Li^+ mobility. However, while Ga^{3+} ions tend to allow limited Li^+ diffusion within their immediate surroundings, the less repulsive interactions associated with Al^{3+} ions lead to a complete blockage of neighboring Li^+ diffusion paths. This effect is magnified at lower temperatures, and explains the higher conductivities observed for Ga-substituted systems. Overall this study provides a valuable insight into the fundamental ion transport mechanism in the bulk of Ga/Al-substituted $Li_7La_3Zr_2O_{12}$ and paves the way for rationalizing aliovalent substitution design strategies for enhancing ionic transport in these materials.

Keywords

Solid electrolytes, Ga/Al-substituted LLZO, Molecular Dynamics, enhanced sampling hybrid Monte Carlo, GSHMC, Li-ion conductivity/diffusion

1 Introduction

From the electrification of transportation (e.g., electric vehicles) to the support of smart grids (e.g., storing wind and solar energy produced during off-peak hours), rechargeable Li-ion batteries are called to create a new energy paradigm. Yet, progress in these fields demands new and improved materials with high ionic conductivities. In particular, in many applications, it is of utmost importance to replace current flammable and toxic organic liquid electrolytes with an inorganic solid alternative, which can offer improved safety by preventing thermal runaway in case of battery failure. Many good Li-ion solid electrolyte candidates crystalize in a few crystal structures: perovskites,[1] NASICON-like,[2] LISICON-like,[3] garnets,[4] and argyrodite.[5] Among them, $Li_7La_3Zr_2O_{12}$ (LLZO) garnet is a strong contender in terms of good Li-ion conductivity,[6,7] wide electrochemical operation window,[8]

and formation of stable interfaces with many cathode materials.[9]

LLZO garnets can crystallize in at least two different polymorphs, a poorly Li-ion conductive tetragonal structure [space group (SG) $I4_1/acd$] and a much more conductive cubic one (SG $Ia\bar{3}d$).[10] More recently, an additional acentric cubic polymorph with SG $I\bar{4}3d$ has also been identified.[11,12] The cubic structure is unstable at room temperature, but it can be stabilized by supervalent substitution at the Li, La, or Zr crystallographic sites. In particular, substitution of Li by Al and Ga ions has extensively been studied, with most efforts focused on elucidating the site preferences of Al and Ga and their effect on Li-ion conduction in LLZO garnets.[13,14] Despite having the same formal charge, Ga substitution is found to lead to higher room temperature conductivities ($\sim 10^{-3}$ S/cm) than Al substitution[11,15–17] ($\sim 10^{-4}$ S/cm). However, the origin and degree of this phenomenon is yet to be fully understood. Recently, Rettenwander et al.[11] combined several characterization techniques to systematically explore the structure and Li-ion conduction properties of Al/Ga dual substituted LLZO garnets, with formula $Li_{6.4}Ga_xAl_{0.2-x}La_3Zr_2O_{12}$, ($x = 0$, 0.05, 0.1, 0.15 and 0.2). They found that the conductivity increases monotonically as x increases (i.e., with increasing Ga content), but the effect tends to vanish as the temperature rises. The observed rise in conductivity with x was attributed to the formation of additional Li-ion diffusion paths for $x \geq 0.15$, caused by a phase transition from centric SG $Ia\bar{3}d$ to acentric SG $I\bar{4}3d$. However, this mechanism does not explain why this trend is observed at all values of x and why it disappears with temperature. Here, we aim to further investigate this phenomenon and gain an atomic-level insight into the different role the similar substitutional metal ions (Al, Ga) have in the bulk Li-ion mobility of LLZO ceramic electrolytes. To tackle this study, force-field-based molecular dynamics (MD) simulations have been applied to a range of model systems and temperatures. In addition to conventional MD simulations, and in order to effectively account for exhaustive sampling at low temperatures, a Generalized Shadow Hybrid Monte Carlo (GSHMC)[18] approach has been applied for the first time to study single and dual substituted LLZO systems.

We focus on three different Ga/Al contents in $Li_{6.4}Ga_xAl_{0.2-x}La_3Zr_2O_{12}$: $x = 0.0$, 0.1 and 0.2. The simplified notation $Ga_xAl_{0.2-x}$ will be used throughout. Hence, the structures to be considered are referred to as $Ga_{0.0}Al_{0.2}$, $Ga_{0.1}Al_{0.1}$, and $Ga_{0.2}Al_{0.0}$. The structure of the pristine cubic-garnet LLZO is shown in Figure 1. Li ions partially occupy 24*d* tetrahedral

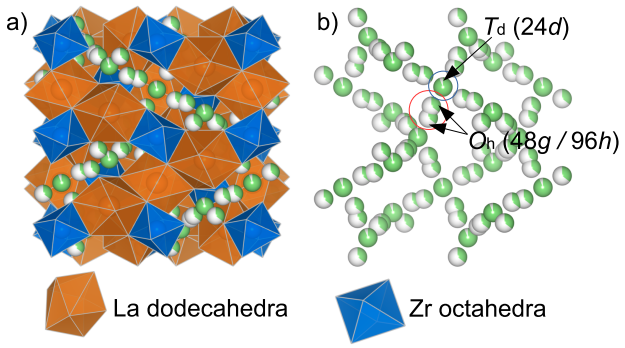

Figure 1: (a) Crystal structure of garnet-type cubic LLZO (SG $Ia\bar{3}d$). Li ions are shown as partially filled spheres, indicating partial occupancy. La dodecahedra and Zr octahedra are depicted in orange and blue, respectively. (b) The Li-ion diffusion pathway, comprising tetrahedral (T_d) 24*d* sites coordinated by 4 octahedral (O_h) 48*g*/96*h* sites.

(T_d) and 48*g*/96*h* octahedral (O_h) sites, La ions fully occupy 24*c* dodecahedral sites, Zr ions fully occupy 16*a* octahedral sites, and O ions fully occupy the 96*h* sites. No definitive consensus exists on the site preferences for Al and Ga ions, with some studies proposing that Ga ions prefer to enrich the 96*h* sites while Al ions occupy 24*d* sites.[19,20] This may be explained by the influence of experimental factors including sample preparation and the synthesis conditions chosen, as discussed in recent experimental works.[13,20] Since the 24*d* sites act as junctions for Li-ion diffusion,[21] this site distribution was originally thought to explain why Ga enhances Li-ion mobility compared to Al. However, recent works locate both Al and Ga ions at 24*d* sites[11,16,22–24] and conclude that no site preferences exist for either.[13,21] Here, we assume that both Ga and Al prefer the T_d sites, as most recent experimental evidence appears to tilt in this direction.

The paper is structured as follows; first, the details of the atomistic model and the force field for $Li_{6.4}Ga_xAl_{0.2-x}La_3Zr_2O_{12}$ are given. Afterward, a series of MD and GSHMC simulations are performed for a set of Al/Ga-substituted LLZO systems to obtain diffusion

dynamics of Li ions. Finally, the predictions gained in this work are compared with available experimental data, in particular, Li-ion diffusivities and conductivities at different temperatures and concentrations of Al/Ga ions in LLZO garnets. Furthermore, we thoroughly examine Li-ion diffusion paths in presence of Al and Ga ions. The results are discussed in the context of the observed experimental enhancement of Li-ion conductivity properties of LLZO electrolytes caused by insertion of Ga over Al ions in $24d$ tetrahedral sites. Our findings reveal an increase in Li-ion conductivity of Ga-substituted bulk LLZO over Al-substituted phases for all temperatures and offer an atomistic insight into the role of Al/Ga ions in the Li-ion transport performance of LLZO electrolytes.

2 Methodology and Computational Details

2.1 Force field derivation

We model the interatomic potential between atoms i and j, U_{ij}, as the sum of Coulombic and van der Waals (vdW) interactions:

$$U_{ij} = \frac{q_i q_j}{4\pi\epsilon|\mathbf{r}_{ij}|} + U_{ij}^{\mathrm{vdW}} \tag{1}$$

where, ϵ is the vacuum permittivity, $|\mathbf{r}_{ij}|$ is the distance between particles i and j, and q_i and q_j are their respective charges. The vdW interaction, U_{ij}^{vdW}, is modeled through the Buckingham potential,

$$U_{ij}^{\mathrm{vdW}} = A_{ij} \exp\left(-B_{ij}\,|\mathbf{r}_{ij}|\right) - \frac{C_{ij}}{|\mathbf{r}_{ij}|^6} \tag{2}$$

with the Buckingham parameters $A_{ij} \geq 0$, $B_{ij} > 0$ and $C_{ij} \geq 0$. While Coulombic interactions are considered between all pairs, only interactions with oxygen atoms are included in U_{ij}^{vdW}. For pristine LLZO, parameters for the force field described by eqs 1 and 2 are readily available.[21,25–27] However, to the best of our knowledge, no parameters have been reported for dual substituted $\mathrm{Ga}_x\mathrm{Al}_{0.2-x}$ systems. Thus, we combined the parameters from

two independent force fields proposed in the literature: one developed by Jalem et al.[21] for Ga-substituted LLZO, and the Al-O potential proposed by Pedone et al.[28] for oxides and silicates. Instead of the Buckingham functional form, Pedone et al.[28] used Morse functions to describe U_{ij}^{vdW}. Therefore, we fitted their Al-O potential to eq 2 in order to extract the required parameters. Unfortunately, the raw parameters extracted from these sources and being used in isothermal-isobaric (NPT) MD simulations could not accurately reproduce the unit cell size of $\mathrm{Ga}_x\mathrm{Al}_{0.2-x}$ reported by Rettenwander et al.[11] for $0.0 \leq x \leq 0.2$ (details of the simulation setup are provided in the following section). Our numerical experiments reveal a sensitivity of the predicted unit cell parameters to a value of the particular force-field parameter, namely B_{ij} for the Li-O interaction, $B_{\text{Li-O}}$. Therefore, by fixing the cubic structure, we chose to fine-tune the parameter $B_{\text{Li-O}}$, until the predicted cell size was within 0.1% of the experimental value for each concentration x. The fine-tuning strategy included the following two steps:

1. **Generation of configurations with minimal potential energy (PE) for each x in $\mathbf{Ga}_x\mathbf{Al}_{0.2-x}$**: A $3 \times 3 \times 3$ supercell (containing 1944 available Li sites, 648 La atoms, 432 Zr atoms, and 2592 O atoms) is considered for the calculation. Even with all Ga and Al ions confined in T_{d} sites, there exists an enormous number of conceivable arrangements of the Li, Li vacancies, Al and Ga within the Li sublattice. A simple sampling approach consists of randomly adjusting the Li/Ga/Al/vacancy arrangements according to the desired stoichiometry.[21,24,29,30] Consequently, for each x, a total of 10000 random structures were generated, and those with the lowest total PE (electrostatic + van der Waals) for each value of x were selected for the subsequent step (the obtained energy distributions are shown in Figure S1 of the SI). Calculations of the PE on the static structures were performed using LAMMPS.[31] This sampling step is carried out only once.

2. **Optimization of $B_{\text{Li-O}}$ for each x**: This task is performed using the minimum PE configuration obtained in the previous step. First, we evaluated the unit cell parameters

using NPT-MD simulations with the current values of the force-field parameters $B_{\text{Li-O}}$. Then we updated $B_{\text{Li-O}}$ and repeated the process until the desired fitting of the MD predicted unit cell parameters into the experimental data is achieved.

Following this optimization procedure, we observe a uniform increase of the unit cell parameter with increase of Ga content; this is expected since only repulsive interactions are included in the Ga-O interatomic potential (see Table S1 of the SI). In consequence, an optimal value of $B_{\text{Li-O}}$ varies with x, and thus it has been decided to assign to each concentration x an x-specific force field. The variation of the optimal $B_{\text{Li-O}}$ with x is depicted in Figure S2 of the SI. In Table S1 of the SI, we show the parameters of the force field (eq 2) used in this study.

2.2 Simulation Setup

Atomistic simulations were carried out with the MultiHMC-GROMACS software code.[32,33] This is an in-house modified version of the open-source MD package GROMACS version 4.5.4[34] which is available under the GNU General Public License. In addition to the algorithms offered by the standard GROMACS package, MultiHMC-GROMACS provides an implementation of various hybrid Monte Carlo (HMC) methods[18,35,36] and multi-stage integration schemes[33,37] with the aim of increasing accuracy and sampling performance of a molecular simulation without a significant loss of computational efficiency and parallel scalability.

In this study we employed two atomistic simulation techniques: MD and GSHMC. GSHMC by Akhmatskaya and Reich[18] is an importance sampling HMC[35] method where sampling is performed with respect to modified Hamiltonians, and stochastic Monte Carlo (MC) proposal steps and MD short trajectories alternate to enhance sampling efficiency. In particular, GSHMC can be viewed as an alternative to HMC which preserves dynamical information and provides high acceptance rates. On the other hand, in contrast to MD, GSHMC rigorously controls temperature and samples much broader due to its stochastic

nature. These features of GSHMC are achieved by (*i*) including a partial update of particle velocities instead of a full velocity resampling between MD trajectories and (*ii*) by sampling with modified Hamiltonians instead of true Hamiltonians. Modified, or shadow Hamiltonians, determined as asymptotic expansions of Hamiltonians in powers of a time step, are better conserved by symplectic integrators than true Hamiltonians which leads to enhanced acceptance rates in GSHMC. The GSHMC method has been successfully employed in the studies of high dimensional configurational spaces and rare events, including simulations of biological systems[32,38–40] and, more recently, ionic diffusion in solid crystalline Na_xFePO_4 systems.[41,42] A complete description of the GSHMC method can be found elsewhere.[18,32,37,40]

In this work, MD and GSHMC simulations have been performed for a range of temperatures from 193 K to 313 K at intervals of 20 K. While at temperatures above 233 K, the preference has been given to MD, due to the simplified tuning of its parameters, at low temperatures ($T \leq 233$ K), we used GSHMC to take advantage of its enhanced sampling abilities, particularly desired at this temperature regime. Sampling efficiency of MD and GSHMC can be estimated through calculation of integrated autocorrelation functions (IACF) during the equilibration stage. Low values of IACFs indicate a lower correlation between generated samples (i.e. more efficient sampling). The calculated IACF values obtained with MD and GSHMC for $Ga_{0.0}Al_{0.2}$, $Ga_{0.1}Al_{0.1}$ and $Ga_{0.2}Al_{0.0}$ at 233 K, 273 K and 313 K are presented in Table S2 of the SI. As observed, GSHMC performs up to 14 times better than MD for the tested systems and temperatures, and the margin of its superiority increases with decreasing temperature.

Periodic boundary conditions were applied in all directions. For both simulation approaches, Coulomb electrostatics were evaluated with the smooth particle mesh Ewald (PME) method[43] taking a cut-off radius of 11 Å. For short-range interactions, a cut-off distance of 12 Å was considered.

Following the energy minimization with the steepest descendent method, the supercells were equilibrated for 500 ps using MD in the NPT ensemble where the average temperature

and pressure where kept constant by the v-rescale algorithm[44] and Andersen barostat[45] at the specified target temperature and pressure P=1 bar, respectively. The production simulations were run in the NVT ensemble, with a total simulation time ranging between 80 and 320 ns depending on the target temperature. The v-rescale thermostat has also been applied in production MD NVT simulations. In contrast to MD, in the GSHMC simulations, temperature is controlled by design in the Metropolis step, while short MD trajectories are performed in the NVE ensemble, therefore, no thermostats are required. In all MD simulations, the velocity Verlet method was used to integrate the particle motion with a time step of 2.5 fs for temperatures above 233 K.

GSHMC was combined with the M-BCSS integrator, the two-stage integrator specially derived for sampling with modified Hamiltonians,[46] for which a time step of 4.0 fs was possible. The parameters to be defined for GSHMC include the length L of MD trajectories, time step Δt, noise parameter ϕ for partial velocity update, and the order of modified Hamiltonian, whereas only time step Δt has to be defined for MD simulations.

To validate the GSHMC parameters, we ran MD and GSHMC simulations with a different set of parameters at a target temperature of 233 K for the $Ga_{0.0}Al_{0.2}$ system. Our calculations revealed that the choice of $L = 250$, $\Delta t = 4.0$ fs, $\phi = 0.5$ and a 4^{th} order modified Hamiltonian for GSHMC, keeps the average temperature (T), kinetic energy (K) and potential energy (U) in good agreement with the data obtained from the MD simulations. For low temperatures investigated in this study, long simulation runs (>300 ns for the lowest temperature) were needed in order to obtain accurate estimates of the transport parameters. A thorough search for the relevant literature confirms that this is the first time when the low temperature regime in LLZO garnets is studied using atomistic simulations, with previous works focusing on very high temperatures[21] or exploring only room temperature conditions.[27] Simulations were performed on 24-core Intel nodes with RAM capacities of 384 GB.

3 Results and Discussion

3.1 Li-ion Transport as a Function of Temperature and Ga/Al Content

Thermal expansion/contraction of Ga/Al substituted LLZO has been calculated for temperatures between 193 K and 313 K for $Ga_{0.0}Al_{0.2}$, $Ga_{0.1}Al_{0.1}$ and $Ga_{0.2}Al_{0.0}$. Our calculations reveal that increasing Ga content produces a subtle expansion of the unit cell volume at all investigated temperatures (see Figure S3 of the SI). This behavior is in agreement with experimental results at room temperature reported by Rettenwander et al.,[11] where a comparison between the experimental lattice parameters and our predictions at 293 K shows a discrepancy of less than 0.1% for all studied Al/Ga concentrations in LLZO. In Table 1, calculated lattice parameter for the investigated $Ga_xAl_{0.2-x}$ systems are shown (differences are less than 0.5%).

Table 1: Experimental and calculated (this work) lattice parameters of $Ga_xAl_{0.2-x}$.

Composition	a (Å)	ref.
$Ga_{0.0}Al_{0.2}$	12.9894(2)	11
	13.0458	47
	12.9681	48
	12.9652(4)	12
	12.9893	this work
$Ga_{0.1}Al_{0.1}$	12.9905(2)	11
	12.9892	this work
$Ga_{0.2}Al_{0.0}$	12.9936(2)	11
	12.9736(1)	12
	12.9733(6)	49
	12.9945	this work

Mean-squared displacements (MSDs) of Li ions at $Ga_{0.2}Al_{0.0}$ for temperatures between 193 K and 313 K are shown in Figure 2. Simulations at $T \geq 233$ K were performed with MD in the NVT ensemble, whilst at $T \leq 233$ K, GSHMC simulations were used with the parameters reported in the previous section. Diffusive motion of Li ions can be identified from those regions in the log-log plot where the slope is approximately unity. As expected, Li

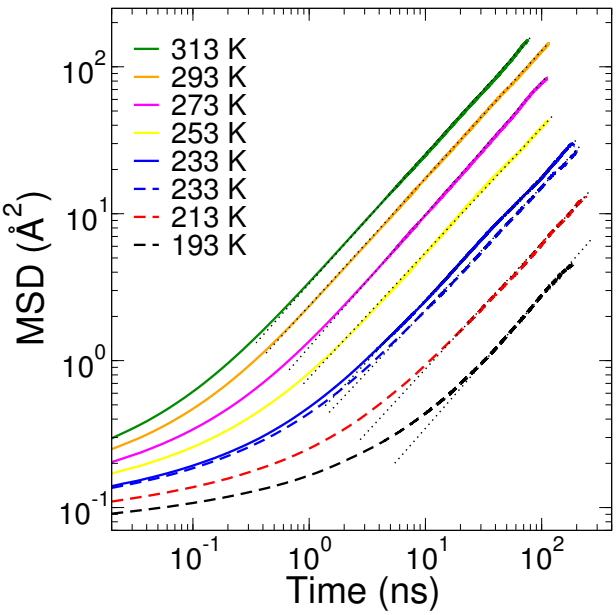

Figure 2: Calculated MSDs of Li ions in $Ga_{0.2}Al_{0.0}$ as a function of simulation time at temperatures between 193 and 313 K. Colored solid and dashed lines represent MD and GSHMC results, respectively. Black dotted lines are the linear fitting in the log-log scale identifying the diffusive regime.

ions move faster at high temperatures while their mobility progressively decreases by orders of magnitude with lowering temperature. This trend is independent of the use of GSHMC or MD simulations. We have included MSDs obtained from MD and GSHMC simulations at 233 K to facilitate the comparison between Li-ion diffusion across LLZO garnets modeled by both methods, revealing similar behaviors at the target temperature. However, differences are expected to increase considerably when lowering temperature. A higher, up to 14 times, sampling efficiency of GSHMC compared to MD demonstrated in Table S2 of SI ultimately has to result in a better capture of dynamic properties at low temperatures.

In Figure 3 we provide an atom's eye view of Li-ion transport by considering a complete trajectory of a selected Li ion across simulations at different temperatures and total time lengths. As expected, Li-ion transport is isotropic. At 313 K, the selected Li ion crosses frequently different T_d and O_h sites in a relatively short lapse of time (80 ns). In addition, we notice that a Li ion can visit the same T_d site several times, as revealed by the presence of branches centered in the nodal T_d sites along the diffusive path as shown in the inset of

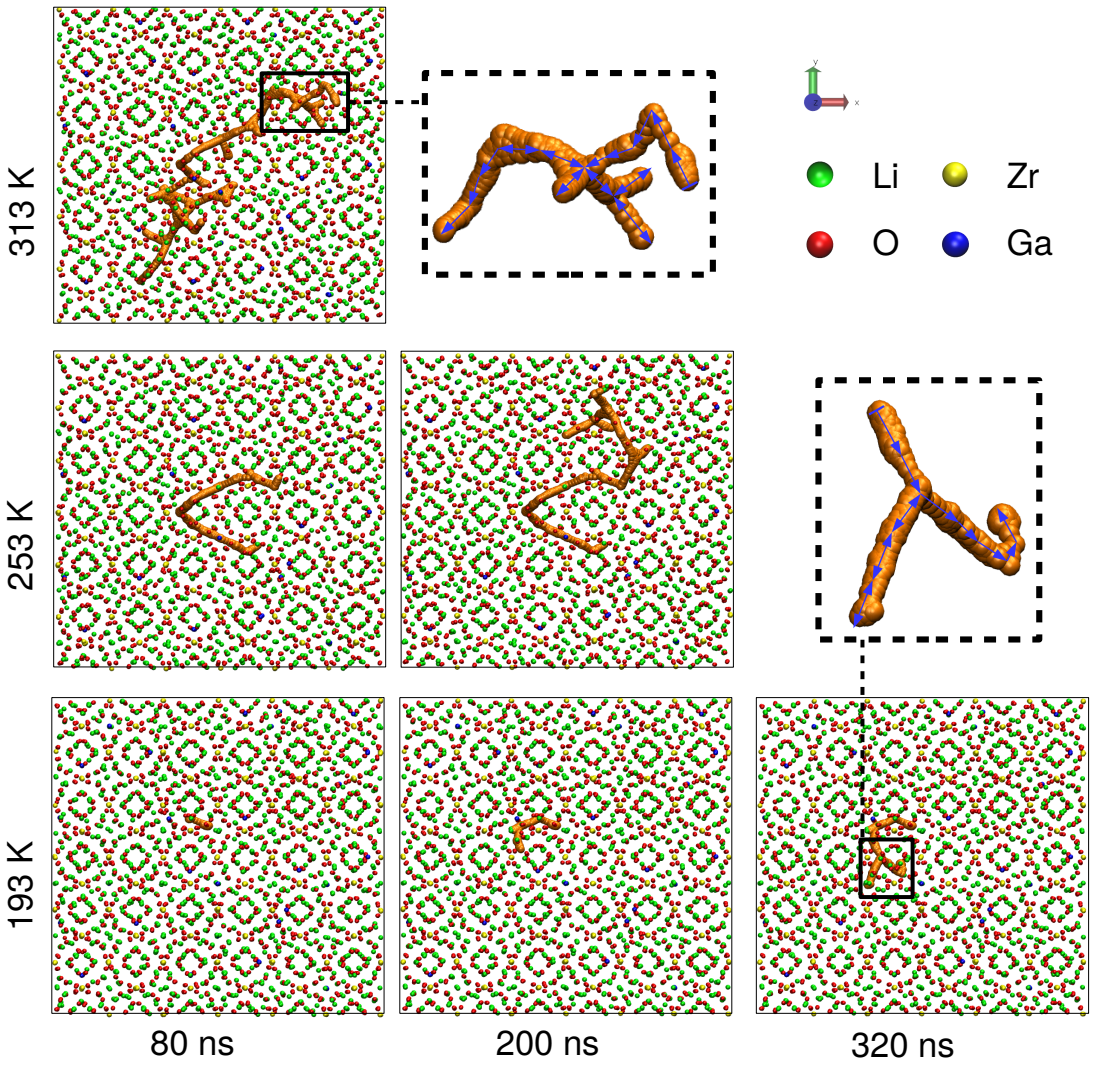

Figure 3: Simulated trajectories of an individual Li ion (orange) in the $Ga_{0.2}Al_{0.0}$ lattice at different temperatures. From top to bottom the temperature decreases, whereas from left to right the simulation time increases. Li, Zr, O and Ga ions are depicted in green, yellow, red and blue spheres, respectively (La ions are not shown for simplicity).

Figure 3. When the temperature is decreased to 253 K, the distance covered by the Li ion in 80 ns decreases. In fact, even after 200 ns the number of $T_{\rm d}$ and $O_{\rm h}$ sites visited has decreased considerably in comparison with the simulation at 313 K, resulting as well in a lower number of branches along the diffusive path. Finally, at 193 K we see that diffusion is severely hindered, with the Li ion barely visiting more than one $T_{\rm d}$ site in less than 80 ns.

To better understand Li-ion diffusion across the LLZO garnet in a collective manner, we systematically monitored the motion of individual labeled Li ions through the diffusion coefficient, $D_{\rm Li}$, which is calculated from the MSD according to,

$$D_{\rm Li} = \lim_{t\to\infty} \frac{1}{6t} \langle |\mathbf{r}_i(t) - \mathbf{r}_i(0)|^2 \rangle_i \tag{3}$$

where $\mathbf{r}_i(t)$ is the position of Li ion i at time t. Figure 4 depicts the temperature dependence of the diffusion coefficients of Li ions in LLZO garnets with different contents of Al and Ga dopants between 198 K and 313 K. The diffusion coefficient follows an Arrhenius-type

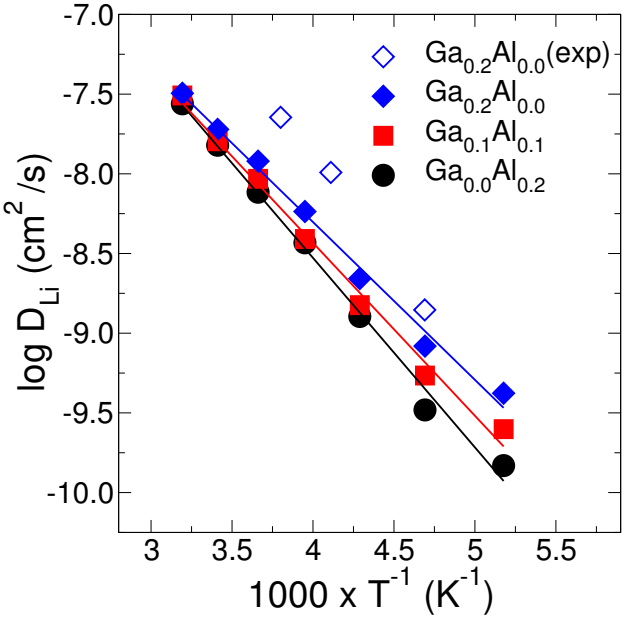

Figure 4: Calculated Li-ion diffusivity as a function of temperature for $\mathrm{Ga}_x\mathrm{Al}_{0.2-x}$ (x = 0.0, 0.1, 0.2). Filled data points refer to simulation data in the bulk region (error bars smaller than symbols). Experimental values, represented by empty diamonds, correspond to $\mathrm{Ga}_{0.2}\mathrm{Al}_{0.0}$ and were taken from Ref. 49.

temperature dependence for all the examined Al/Ga contents. This behavior has also been reported in MD simulations of Li-ion diffusion in Ga-substituted LLZO[21] and $Li_5La_3Ta_2O_{12}$ garnets.[50] In addition, this trend is similar to the one observed in experiments for LLZO garnets containing Al,[22,23] Ga[49] and Ta[51] ions. In particular, by using alternating current impedance experiments, Wu et al.[49] found $Ga_{0.2}Al_{0.0}$ diffusivities to be between 10^{-9} and 10^{-8} cm^2/s at temperatures between 213 and 263 K; these values are above the ones reported in this work, where for the 213 - 253 K temperature range, the estimated diffusion coefficients are of $\sim 10^{-9}$ cm^2/s. Diverse effects can be the cause of the discrepancy between experimental and simulated diffusivities. On the one hand, MC and MD simulations of pristine LLZO systems have revealed a difference up to 2 orders of magnitude in diffusivity when comparing motion of Li ions in the grain boundary (GB) and bulk regions at 300 K for three GB geometries.[52] A similar observation was reported by Dawson et al.[53] for polycrystalline electrolyte Li_3OCl, where Li-ion MSD curves exhibit differences for bulk and GB diffusivities at 700 K. Additionally, when considering more local experimental techniques, such as NMR[22,54] and muon spin relaxation spectroscopy[23] on Al-substituted LLZO, differences can be of several orders of magnitude in measurements of the diffusion constant at similar temperatures.

Our results indicate that the Li-ion diffusivity in the bulk of the LLZO structure (i.e. not considering the GBs), decreases as the Al content increases, which is corroborated by comparing experimental data for fully Al-[22,23,54] and Ga-[49] substituted LLZO. This is expected to affect the conductivity and voltage stability of doped LLZO garnets. In consequence, it is of utmost importance to understand how the presence and proportion of Ga/Al ions affect the structure, path topology and Li-ion dynamics.

3.2 Pathways of Li-ion Diffusion

Figure 5 shows the maximum displacement per particle (MDPP) for Li ions in the $Ga_{0.0}Al_{0.2}$ and $Ga_{0.2}Al_{0.0}$ systems at 233 K and 313 K after 192 ns and 40 ns simulation runs, respectively. It is important to remark that this plot was made using the "unwrapped" Li-ion

coordinates and thus, it is not affected by the boundary periodicity. Naturally, the MDPP increases with temperature. However, the MDPP differences between the $Ga_{0.0}Al_{0.2}$ and $Ga_{0.2}Al_{0.0}$ curves are more significant at 233 K than at 313 K. At 233 K, nearly the same number of Li ions ($\sim$ 45%) are unable to jump into an adjacent site for both structures (Li ions with MDPP under the yellow dashed line). Nevertheless, once this threshold is crossed, the Li ions in $Ga_{0.2}Al_{0.0}$ can move, in average, a longer distance than in $Ga_{0.0}Al_{0.2}$. For example, $\sim$ 37% of Li ions are able to cover at least one T_{d} length for $Ga_{0.2}Al_{0.0}$, while this fraction reduces to $\sim$ 30% for $Ga_{0.0}Al_{0.2}$ (particles with MDPP above the blue dashed line). Moreover, $\sim$ 20% of Li ions in $Ga_{0.2}Al_{0.0}$ are able to cross at least two T_{d} sites, but only $\sim$ 12% of Li ions in $Ga_{0.0}Al_{0.2}$ are able to do likewise (particles with MDPP above the magenta dashed line). At 313 K the differences are less remarkable, with the fraction of Li ions displacing less than 7.3 Å being identical for both structures ($\sim$ 57%). These numbers are simulation length-dependant; however, they suggest two important insights: (*i*) at a given temperature, nearly the same number of Li ions are trapped (cannot move to adjacent sites) in Ga- and Al-substituted LLZO, (*ii*) mobile Li ions move in average a longer distance in Ga-substituted than in Al-substituted LLZO, but this difference tends to vanish as the temperature increases.

In order to further understand the implications of these new insights, we first recall some general conclusions from previous works in the literature. Using DFT calculations, Rettenwander et al.[11] found that Ga raises the site energy of the neighboring T_{d} site by 10 meV higher than Al. Since the O_{h} sites are more energetic than the T_{d} sites,[55] this energy increase smooths the energy landscape and facilitates diffusion. Indeed, Al is less repulsive than Ga (the attractive term in our Al-O Buckingham potential is nonzero), and it is therefore expected that Ga smooths the energy landscape more than Al. Similarly, Rettenwander et al.[11] proposed that an additional diffusion path is activated for $Ga_{x\geq 0.15}Al_{0.2-x}$ when a phase transition from $Ia\bar{3}d$ to $I\bar{4}3d$ occurs. In this scenario Li ions are allowed to bypass the $12a$ junction (equivalent to $24d$ in $Ia\bar{3}d$) and perform direct jumps between octahedrally

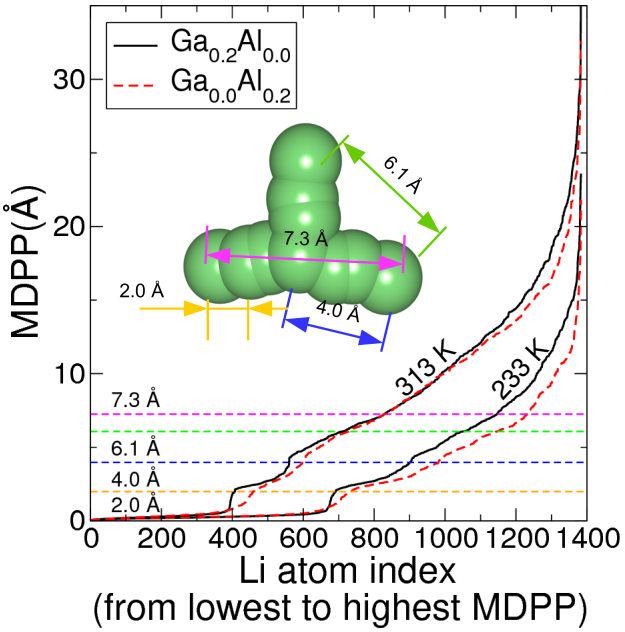

Figure 5: MDPP for $Ga_{0.0}Al_{0.2}$ and $Ga_{0.2}Al_{0.0}$ at 233 K and 313 K after 192 ns and 40 ns simulation run, respectively. The Li-ion indexes (horizontal axis) are ordered from lowest to highest total displacement (vertical axis). The inset displays the geometry and characteristic lengths of the Li-ion diffusion path: T_d site-nearest O_h site (2 Å), T_d site-nearest T_d site (4 Å), T_d site-second nearest T_d site (6.1 Å), T_d site-third nearest T_d site (7.3 Å). These characteristic lengths are illustrated in the MDPP plot through the horizontal dashed lines.

coordinated 48e sites (similar to 96h in $Ia\bar{3}d$). Our results, however, suggest that both Ga and Al tend to hinder the mobility of a significant number of Li ions at any dopant concentration. To further examine this apparent disagreement, we depict the Li-M (M = Al or Ga) radial distribution function, $g(r)$, for $Ga_{0.2}Al_{0.0}$ and $Ga_{0.0}Al_{0.2}$ at 233 K for four subsets of Li ions: Li(all), corresponding to all Li ions in the system (Figure 6a); Li(<2 Å), corresponding to those Li ions displacing less than the minimum T_d-O_h distance of 2 Å (Figure 6b); Li(>2 Å), corresponding to those Li ions displacing *at least* the minimum T_d-O_h distance of 2 Å (Figure 6c); and Li(>4 Å), corresponding to those Li ions displacing *at least* the minimum T_d distance of 4 Å (Figure 6d). Notice that $g_{\text{Li(all)-M}}(r) = g_{\text{Li(<2 Å)-M}}(r) + g_{\text{Li(>2 Å)-M}}(r)$.

Figure 6a reveals that the distributions of Li ions around tetrahedrally coordinated Ga and Al ions are similar, although the first peak corresponding to the nearest occupied O_h site is $\sim$ 0.3 Å closer to Al ion than to Ga ion, as a consequence of the larger size of the latter. The nearest T_d site, corresponding to the second peak, is located $\sim$ 3.9 Å from the central cation in both cases, and its occupancy is evidently higher than that of the nearest O_h site. The blue arrows represent peaks whose relative magnitude drop with respect to that shown in Figure 6a. The three peaks at $r \leq 5$ Å reduce considerably in Figures 6c and 6d, indicating that diffusion is highly constrained in the vicinity on Al/Ga atoms. On the contrary, these peaks are enhanced in Figure 6(b), corroborating the occurrence of Li entrapment up to the neighboring T_d site of a Ga/Al ion. As a consequence, a significant fraction of diffusion paths that include T_d sites neighboring Ga/Al ions are interrupted. However, the magnitude of such entrapment is not identical for Ga and Al.

Indeed, volumetric integration of $g_{\text{Li(all)-M}}(r)$, between 0 and 3.45 Å (vertical dotted line in Figure 6) yields an average number of Li, $\langle n_{\text{Li(all)}} \rangle^{\text{M}}$, of 1.39 and 1.11 for Al and Ga, respectively. This means that in the case of Ga ions, only one of the nearest O_h sites is generally occupied. In contrast, for Al ions, between one and two of these sites are occupied. On the other hand, integrating between 3.45 Å and 4.45 Å (distances between the dotted

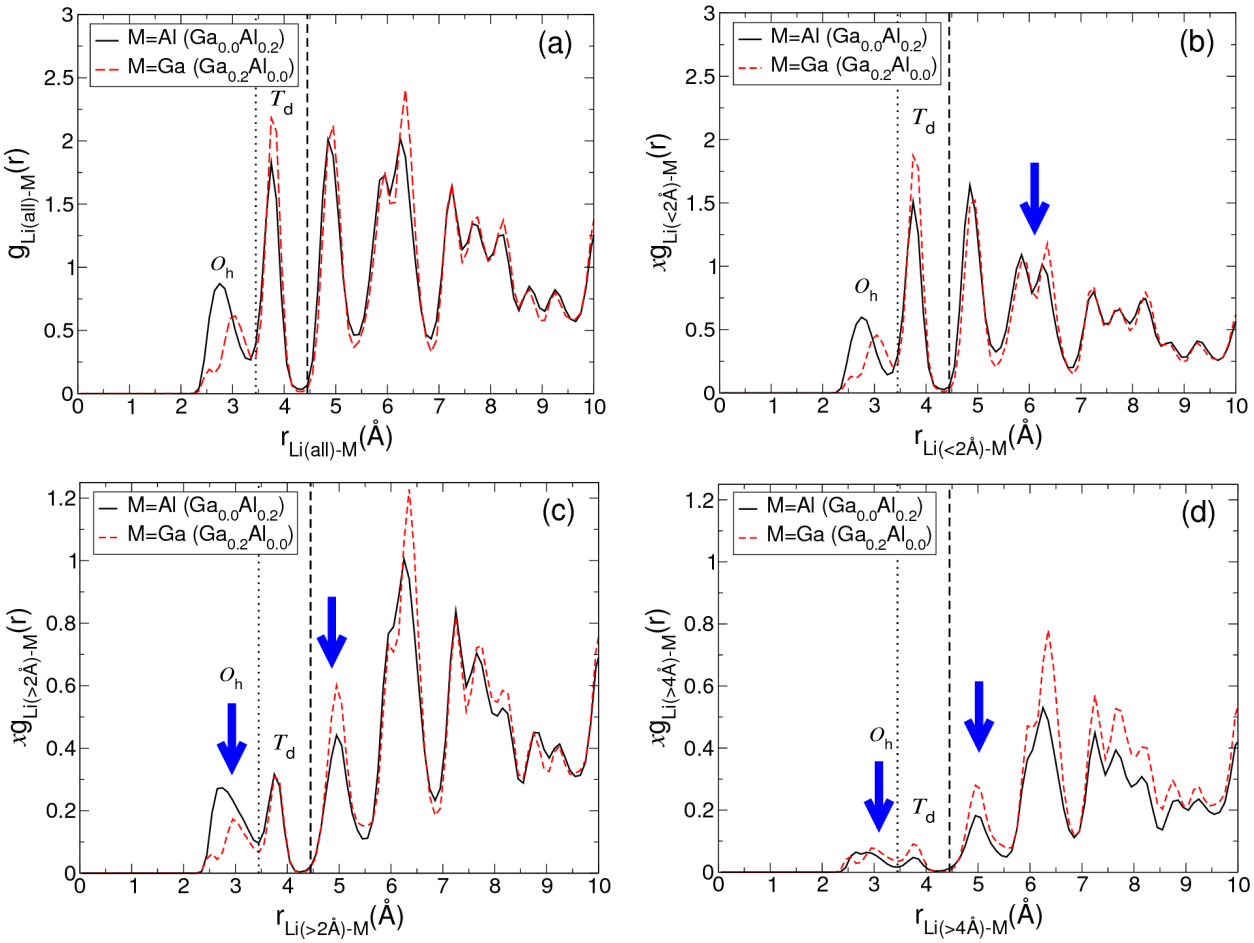

Figure 6: Li-M (M = Al or Ga) radial distribution functions averaged over 192 ns for $Ga_{0.2}Al_{0.0}$ and $Ga_{0.0}Al_{0.2}$ at 233 K, including (a) all Li in the system, Li(all); (b) only those Li remaining within their initial site (i.e., Li ions displacing less than 2 Å, Li(<2 Å)); (c) only those Li jumping at least to one adjacent site (i.e., Li ions displacing more than 2 Å, Li(>2 Å)); and (d) only those Li ions jumping at least the distance between two T_d sites (i.e., Li ions displacing more than 4 Å, Li(>4 Å)). In every case, the $g(r)$ is scaled by the fraction x of Li ions in each subset. The peak before the dotted vertical line corresponds to the nearest O_h sites to the Al/Ga dopant, whereas the peak between the dotted and dashed vertical lines corresponds to the nearest T_d sites. While the absolute height of the peaks differ from (a)-(d), their relative heights reveal the effect of Ga/Al presence on T_d sites. The blue arrows point towards peaks whose relative magnitudes drop with respect to that shown in (a).

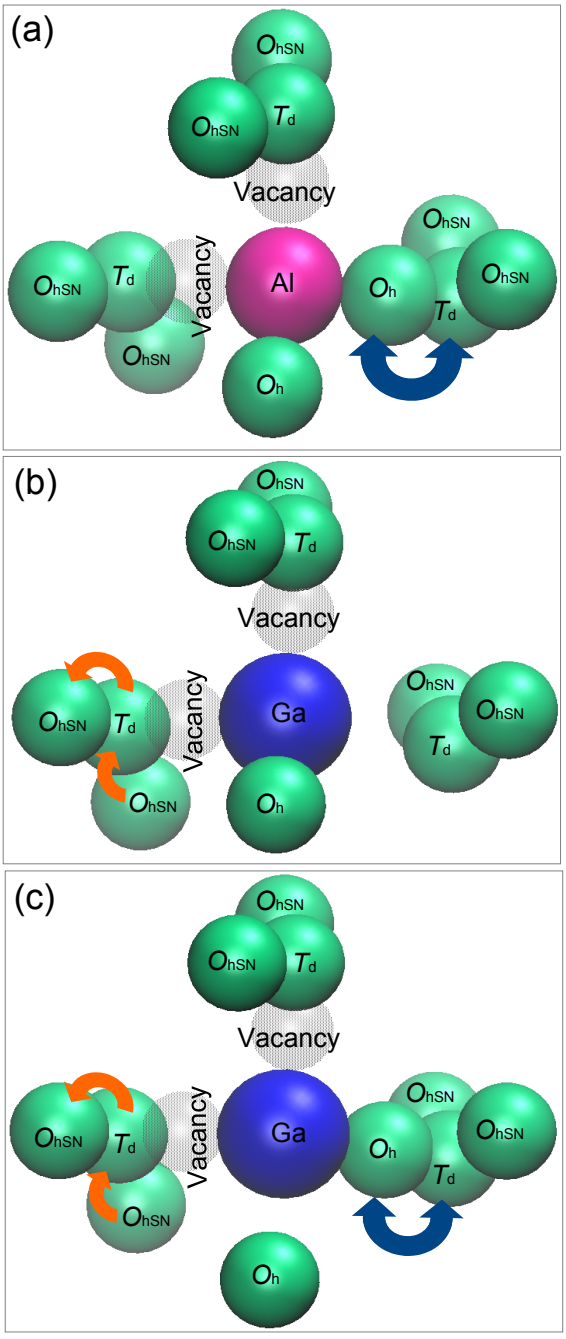

Figure 7: Scheme of the environment surrounding an Al ion (a) and a Ga ion (b,c) in LLZO. Labels T_{d} and O_{h}, represent the nearest Li ions in T_{d} and O_{h} sites to the central cation, respectively, while O_{hSN} stand for the second nearest octahedral sites.

and dashed vertical lines) produces $\langle n_{\mathrm{Li(all)}}\rangle^{\mathrm{Al}} = 2.87$ and $\langle n_{\mathrm{Li(all)}}\rangle^{\mathrm{Ga}} = 3.20$ at the nearest T_{d} sites. Although these numbers correspond to about three Li ions, it indicates that, in a few instances, an Al ion would have only two, while a Ga atom would have 4 $\mathrm{Li}_{T_{\mathrm{d}}}$ neighbors at this position. In order to facilitate interpretation, Figure 7a represents the idealized situation in which all Al cations have the same relative distances to surrounding Li ions. In that case, $\langle n_{\mathrm{Li(all)}}\rangle^{\mathrm{Al}} = 2.87$ can be understood as two nearest T_{d} sites having a 100% occupancy, and one additional T_{d} site having a 87% occupancy. Since all Al ions are assumed to be identical, a partial occupancy is a sign of Li-ion mobility. Performing similar integrations on $g_{\mathrm{Li(<2\ \text{Å})\text{-}Al}}(r)$ (Figure 6b), leads to $\langle n_{\mathrm{Li(<2\ \text{Å})}}\rangle^{\mathrm{Al}} = 0.91$ in the nearest O_{h} sites, and to $\langle n_{\mathrm{Li(<2\ \text{Å})}}\rangle^{\mathrm{Al}} = 2.34$ in the nearest T_{d} sites. Given that these values correspond to Li ions that do not displace to an adjacent site, and considering that $\langle n_{\mathrm{Li(all)}}\rangle^{\mathrm{Al}} = 1.39$ and 2.87 for the O_{h} and T_{d} sites, respectively, we suggest that about one O_{h} site is permanently occupied by a Li ion, while another Li ion jumps back and forth between two nearest O_{h} and T_{d} sites. Indeed, integrating $g_{\mathrm{Li(>2\ \text{Å})\text{-}Al}}(r)$ in Figure 6c leads to $\langle n_{\mathrm{Li(>2\ \text{Å})}}\rangle^{\mathrm{Al}} \approx 0.5$ for both the nearest O_{h} and T_{d} sites, an indication that a mobile Li ion spends half of its time on a O_{h} site and the other half on an adjacent T_{d} site. However, there is no long range diffusion in the nearest vicinity of an Al ion: integrating $g_{\mathrm{Li(>4\ \text{Å})\text{-}Al}}(r)$ in Figure 6d produces $\langle n_{\mathrm{Li(>4\ \text{Å})}}\rangle^{\mathrm{Al}} \approx 0.1$ for the nearest O_{h} and T_{d} sites; that is, no diffusion path exists within 4 Å of an Al ion. In addition, since two T_{d} sites are permanently occupied, it is likely that the vacancies generated by Al substitution remain in empty O_{h} sites adjacent to the Al ion. These conclusions are summarized in Figure 7a: the double blue arrow indicates that a Li ion moves alternatively between nearest T_{d} and O_{h} sites, but no long range diffusion occurs; the gray spheres constitute the permanent locations of the Li vacancies nearest to Al.

Based on the above interpretation, every Al atom blocks in average five junctions (4 nearest $\mathrm{Li}_{T_{\mathrm{d}}}$ neighbors + 1 $\mathrm{Al}_{T_{\mathrm{d}}}$ site). Such effect appears to be synergistic, with two or more Al ions within 6 Å from each other causing a considerable disruption of the available diffusion paths, as we will show later. Interestingly, the second nearest O_{h} sites, O_{hSN} (peak

at 5 Å in the $g(r)$), present low availability for long range diffusion, with $\langle n_{\mathrm{Li}(>4\ \text{Å})}\rangle^{\mathrm{Al}} = 0.70$. On the one hand, every Li ion jumping onto one of these sites must reverse its path due to the aforementioned junction blocking. On the other hand, at 5 Å the attractive short range forces from Al ions are still significant, and might reduce the ability of Li ions to perform the path reversal.

An analogous analysis can be performed for Ga. Integrating the $g(r)$ curves for Ga-Li (red dashed lines in Figure 6) between 0 and 3.45 Å, yields the average number of Li ions at the nearest O_{h} sites to the Ga cation. Performing this integration on Figures 6a, 6b, and 6c yields $\langle n_{\mathrm{Li(all)}}\rangle^{\mathrm{Ga}} = 1.0$, $\langle n_{\mathrm{Li}(<2\ \text{Å})}\rangle^{\mathrm{Ga}} = 0.72$, and $\langle n_{\mathrm{Li}(>2\ \text{Å})}\rangle^{\mathrm{Ga}} = 0.28$, respectively. This result can be interpreted in the following way: there is in average one occupied O_{h} site around each Ga ion. However, 72% of Ga ions have one permanently occupied O_{h} site with a fixed Li ion (Figure 7b), while 28% of Ga have a mobile Li ion instead. In order to assess long range diffusion in the mobile Li ion, we integrate the Ga-Li $g(r)$ curve in Figure 6d between 0 and 3.45 Å, obtaining $\langle n_{\mathrm{Li}(>4\ \text{Å})}\rangle^{\mathrm{Ga}} = 0.09$. This suggest that the mobile Li ion at the O_{h} site is occasionally moving to the adjacent T_{d} site, but is unable to undergo long range diffusion (see sketch in Figure 7c).

When the integration of the Li-Ga $g(r)$ curves is performed between 3.45 Å and 4.45 Å, the average number of Li ions at the nearest T_{d} sites to the Ga cation is found. These integrations yield $\langle n_{\mathrm{Li(all)}}\rangle^{\mathrm{Ga}} = 3.20$ (from Figure 6a), $\langle n_{\mathrm{Li}(<2\ \text{Å})}\rangle^{\mathrm{Ga}} = 2.74$ (from Figure 6b), $\langle n_{\mathrm{Li}(>2\ \text{Å})}\rangle^{\mathrm{Ga}} = 0.46$ (from Figure 6c), and $\langle n_{\mathrm{Li}(>4\ \text{Å})}\rangle^{\mathrm{Ga}} = 0.18$ (from Figure 6d). In order to interpret these values, it must be considered that the occupied O_{h} site in Figure 7b would prevent occupancy at the adjacent T_{d} site (because simultaneous occupancy would lead to atomic overlapping). Since the number of fixed Li ions at T_{d} sites is 2.74, we can assign to every Ga cation at least two fixed Li ions at the nearest T_{d} sites (holding the Ga associated vacancies). Now, because $\langle n_{\mathrm{Li}(>2\ \text{Å})}\rangle^{\mathrm{Ga}} = 0.46$, 46% of Ga can be described as having a mobile Li-ion at a T_{d} site. Since it was established in the previous paragraph that in 28% of the cases a Li ion is moving back and forth between adjacent T_{d} and O_{h} sites, it

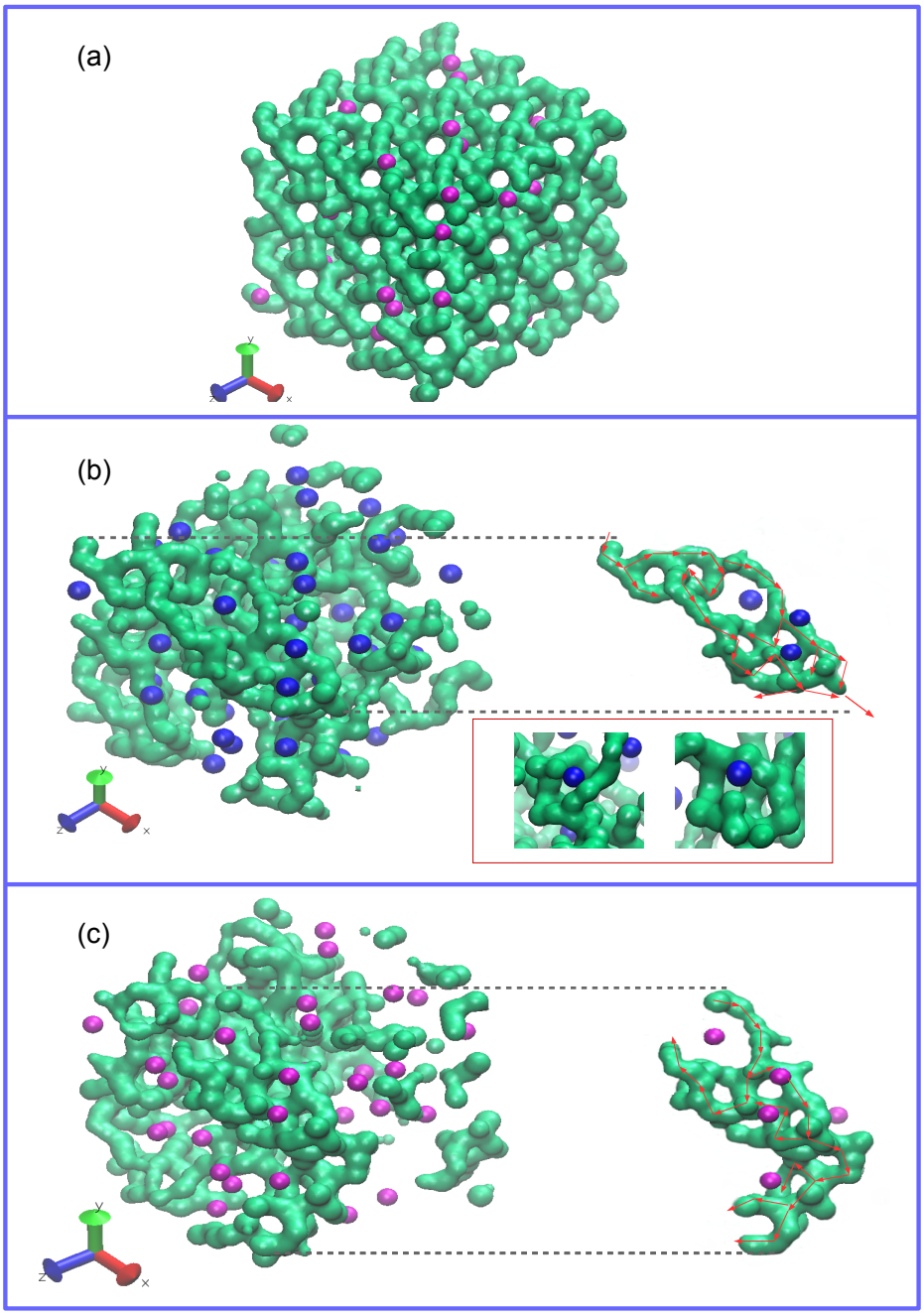

Figure 8: Density volume maps at 233 K for all Li ions (Li(all)) in $Ga_{0.0}Al_{0.2}$ (a), and only those Li ions jumping at least the distance between two adjacent T_d sites in 190 ns (Li(>4 Å)) in $Ga_{0.2}Al_{0.0}$ (b) and $Ga_{0.0}Al_{0.2}$ (c). Al and Ga ions are represented by magenta and blue spheres, respectively. (a) Can be interpreted as the total available volume for Li-ion diffusion, while (b) and (c) correspond to the active volume where diffusion is actually occurring. The extracts on the right of (b) and (c) constitute diffusion paths traversing the simulation box, indicating that long range ionic transport happens in both cases. Only Ga ions allow, under limited circumstances, the presence of active paths in their immediate surroundings (see inset in (b)).

must be the case that in $46\% - 28\% = 18\%$ of Ga cations (precisely the estimated value of $\langle n_{\mathrm{Li}(>4\ \text{Å})}\rangle^{\mathrm{Ga}}$) a Li ion passing through a T_{d} site neighboring a Ga can diffuse long range. This can be happening in either of the scenarios depicted in Figures 7b or c. In other words, approximately 1 in every 5 Ga has a nearest T_{d} site making part of a long range diffusion path.

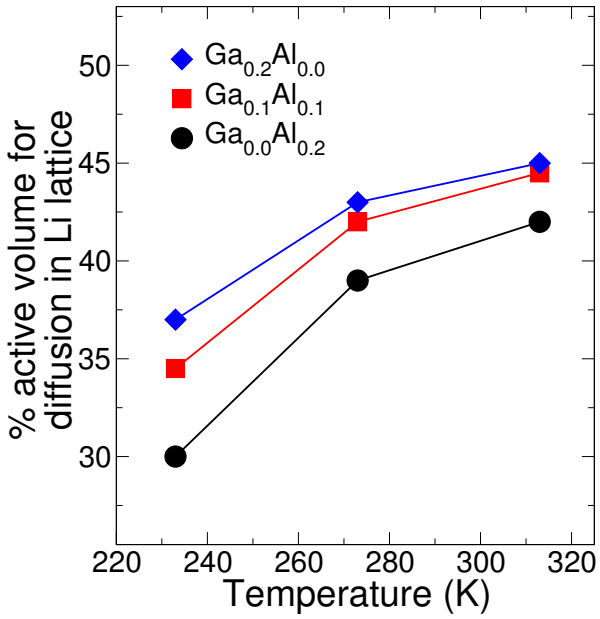

Figure 9: Percentage of volume in the Li lattice that is actively engaged in Li-ion diffusion for $Ga_{0.2}Al_{0.0}$, $Ga_{0.1}Al_{0.1}$, and $Ga_{0.0}Al_{0.2}$ at several temperatures.

Of course, the interpretations given above of the environment around Al/Ga ions are not necessarily unique, because the $g(r)$ results from an ensemble average. Nevertheless, they match well empirical observations from a large number of simulated trajectories, as well as the density volume maps depicted in Figure 8.

The differences in the local environment of Ga and Al can be explained by differences in the short range interactions. The attractive term in the Al-O Buckingham potential ultimately hinders all chances of diffusion around Al. Indeed, at the second nearest O_{h} sites $\langle n_{\mathrm{Li}(>4\ \text{Å})}\rangle^{\mathrm{Ga}} \approx 1.0$, which is 30% higher than $\langle n_{\mathrm{Li}(>4\ \text{Å})}\rangle^{\mathrm{Al}}$. As mentioned above, DFT studies[11] have shown that diffusion in the vicinity of Ga is easier. However, our simulations indicate that such effect only occurs in a minority of Ga ions, probably due to a combination

of two factors: (*i*) the trapped Li vacancies associated to Ga-substitution stabilize Li ions at the nearest T_{d} sites, (*ii*) Li entrapment is intensified at intermediate sites between two or more nearby Ga ions (separated by $\sim$ 8 Å or less). For the configurations examined here, the mean distance between Ga ions at a concentration of 0.2 Ga per formula unit (pfu) is 10 Å, which means that a considerable proportion of Ga ions displays this kind of negative cooperation.

As the temperature increases, the additional kinetic energy allows more Li ions in the vicinity of Al to overcome the effect of attractive non-bonded interactions, reducing the diffusivity/conductivity gap between Al- and Ga-substituted LLZO (see Figure 4 and the MDPP at 313 K in Figure 5). In order to show the overall effect of Ga/Al substitution, Figure 8a depicts the density volume map for Li (all) in $Ga_{0.0}Al_{0.2}$. The picture is identical for $Ga_{0.2}Al_{0.0}$ when diffusing and non-diffusing Li ions are included. However, when only diffusing Li ions, Li(>4 Å), are considered, the differences between Ga- (Figure 8b) and Al- (Figure 8c) substituted LLZO become more significant. While in both cases long range diffusion paths traversing the length of the simulation box are found (examples of which are depicted on the right side of the Figures), there is a greater absence of active paths in the vicinity of Al ions than around Ga ions. In particular, local regions with a cation concentration higher than average, experience the effect of Li entrapment more intensely. Notably, for relatively isolated Ga ions (i.e., with their nearest Ga neighbor at least $\sim$ 10 Å away), active diffusion paths are observed within 4 Å of the Ga ion. Two examples are shown in the inset of Figure 8b. This type of paths are absent in $Ga_{0.0}Al_{0.2}$, where active diffusion paths are always found outside the 4 Å radius of each Al ion. Assuming that the volume of the Li sublattice in Figure 8a corresponds to the total available volume for Li diffusion, we find that 37% of this volume is used in $Ga_{0.2}Al_{0.0}$, and reduces to 30% for $Ga_{0.0}Al_{0.2}$. The difference narrows with increasing temperature, as shown in Figure 9. For instance, at 313 K, 45% and 42% of the available volume in the Li sublattice is used for diffusion in $Ga_{0.2}Al_{0.0}$ and $Ga_{0.0}Al_{0.2}$, respectively. Hence, from a theoretical standpoint, there is little benefit in Ga

substitution over Al substitution at any temperature above 313 K. Of course, differences arising from the density, porosity and grain boundary chemistry can still make one cation more convenient than the other at these relatively high temperatures. Interestingly, the percentage of active volume for diffusion in $Ga_{0.1}Al_{0.1}$ is closer to $Ga_{0.2}Al_{0.0}$ than to $Ga_{0.0}Al_{0.2}$ at all temperatures. This asymmetry suggests that the detrimental collective effect of Al substitution can be readily mitigated by co-substitution of Al with a larger cation.

One important conclusion from the previous discussion is that Li substitution at any concentration above the one necessary to produce the tetragonal to cubic phase transition in LLZO is detrimental to Li conductivity. Indeed, since each cation tends to block between 4 and 5 tetrahedral junctions and trap its associated vacancies, adding Al/Ga would invariably reduce the number of active diffusion paths. This is in line with Travis et al. findings,[56] who conclude that a maximum Li-ion conductivity in Ta-substituted LLZO is reached at a concentration of 6.5 Li pfu, solely due to complete transition from tetragonal to cubic LLZO. A maximum in Ga-substituted LLZO conductivity has been determined by several authors at different Ga concentrations. Bernuy-Lopez et al.[16] measured a maximum in conductivity of 1.3 mS/cm at 0.15 Ga pfu, while Wu et al.[49] obtained a maximum of 1.46 mS/cm with 0.25 Ga pfu. On the other hand, Jalem et al.[21] estimated through force field calculations that a maximum of 1.42 mS/cm occurred around 0.02 Ga pfu. However, there is no consensus regarding the concentration of Ga required for full phase transition from tetragonal to cubic LLZO at room temperature. In addition, while Rettenwander et al.[20] found through X-ray diffraction that at concentrations as low as 0.08 Ga pfu Ga-substituted LLZO is found in the cubic phase, Wu et al.[49] determined through coupled plasma optical emission spectroscopy that below 0.20 Ga pfu a combination of tetragonal and cubic phases exists, with complete transition occurring only above this concentration. Therefore, it is unclear to which degree the maximum is a consequence of the phase transition, or additional effects (e.g., volumetric expansion due to additional electrostatic repulsion). Moreover, the maximum Ga content that can be incorporated into the garnet can be affected by the synthesis route. Thus, while

Rettenwander et al.[20] observed Ga contents up to 0.53 pfu in LLZO garnets, Shinawi and Janek[57] achieved only small concentrations of Ga ions in LLZO due to segregation into the grain boundaries. In all cases, the maximum appears to be very close to the concentration at which the transition has been measured, making the exploration of high Ga pfu concentrations[13,20] very challenging.

3.3 Li-ion Conductivity in Bulk Structure

The conductivity in the bulk is related to the diffusion coefficient of Li ions through the Nernst-Einstein relation,

$$\sigma_{\mathrm{Li}} = \frac{c\,(zF)^2\,D_{\mathrm{Li}}}{RT} \tag{4}$$

where c is the concentration of ionic species with ionic charge z, F the Faraday's constant, R the gas constant, and T the temperature. The conductivities predicted in this work together with experimental data available in Ref. 11 are displayed in Figure 10. According to the

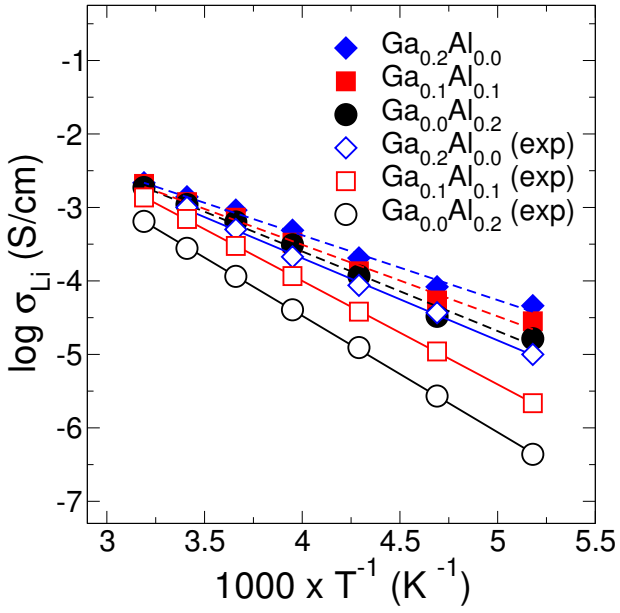

Figure 10: Li-ion temperature-dependent bulk (or grain) conductivities for $Ga_xAl_{0.2-x}$ at different Al/Ga concentrations. Conductivities calculated from simulations are represented by filled symbols connected by dashed lines (error bars smaller than symbols). Experimental data points (empty symbols linked with solid lines) were taken from Ref. 11 and correspond to samples with relative densities close to 85%.

simulations, the bulk conductivity decreases with decreasing temperature for all values of x in $Ga_xAl_{0.2-x}$. The same behavior is found in experimental works based on impedance spectroscopy for Al-[11,22,23,58–62] and Ga-substituted[11,24,49,59,63,64] LLZO systems. Although the overall trend in conductivity is independent of the substituent cation, this is not the case for the corresponding slopes which are related to the activation energies. Indeed, the activation energy calculated from the slope of $\log(\sigma T)$ vs T^{-1} in Figure 10 increases, going from 196 meV to 236 meV for $Ga_{0.2}Al_{0.0}$ and $Ga_{0.0}Al_{0.2}$, respectively, as the content of Al increases, as also has been observed experimentally.[11] Consequently, the difference between the conductivities of Al-substituted and Ga-substituted LLZO systems decreases with temperature increasing. According to our calculations, this occurs because the difference in the fraction of available volume for Li ions to propagate in LLZO garnet increases as the temperature decreases (Figure 9), going from 45% in $Ga_{0.2}Al_{0.0}$ and 42% in $Ga_{0.0}Al_{0.2}$ at 313 K to 37% and 30% in $Ga_{0.2}Al_{0.0}$ and $Ga_{0.0}Al_{0.2}$ at 233 K, respectively.

Though our results capture the main qualitative behavior of conductivity, Figure 10 shows that our predictions overestimate the experimental values from Rettenwander et al.[11] over the whole range of temperatures. Notably, the difference between the simulated and experimental data reduces as the content of Ga increases, suggesting that the Ga-rich samples synthesized by Rettenwander et al. tend to approximate better the ideal crystal structures investigated in our simulations. Indeed, Rettenwander et al. indicated that while Ga-rich LLZO displayed denser microstructures with better connected grains and smaller pores, Al-rich LLZO lead simultaneously to more pronounced separation of grains and increased grain sizes. The difficulty of producing dense Al-substituted garnets has been previously reported, and new synthesis methods have been developed to overcome this problem.[17,65,66] Nevertheless, incorporation of Ga ions appears to lead in general to better grain connectivity upon sintering,[12,67] compared to Al-substituted garnets, and may be an important reason for the better agreement between experimental and simulated data observed for Ga-substituted systems.

In order to thoroughly assess the accuracy of our predictions, we reviewed the available experimental data and identified two factors that make it problematic to perform a direct comparison of the conductivities obtained from experiments and simulations:

Sample density: Higher garnet pellet relative densities tend to increase the conductivity. Matsuda et al.[59] used impedance spectroscopy to show that decreasing the density of $Ga_{0.25}Al_{0.0}$ samples from 94% to 91%, reduced the bulk and total conductivities by 6% and 33% at 298 K, respectively. Similarly, Yang et al.[64] synthesized Ga-substituted LLZO samples with relative densities of 98% and 90% using different methods. Impedance measurements produced one order of magnitude differences between the total conductivities of both samples. Given that all Rettenwander et al.[11] samples have a density close to 85%, it is not surprising that our predictions overestimate the reference experimental values in Figure 10. For pristine LLZO, large variations in the conductivity with relative density were reported by Yunsung and co-workers.[68]

Synthesis conditions: While synthesis conditions can affect pellet density, they also influence the purity, particle size and GB chemistry. For instance, the effect of moisture in LLZO results in Li^+-H^+ exchange, immobilizing part of the Li ions. Similarly, exposure of LLZO to CO_2 from air forms Li_2CO_3, which is insulating and tends to segregate at the GB regions. More recently, Cheng et al.[62] reported total conductivities at 298 K three times higher for pellets processed in Argon atmosphere in comparison with samples sintered in air. In addition, Yang et al.[64] determined that total conductivities may vary from $\sim 10^{-3}$ to $\sim 10^{-4}$ S/cm at temperatures below 358 K for Ga-substituted LLZO pellets synthesized by Couette-Taylor or batch reactors, respectively.

To summarize, experimental conductivity data might be strongly influenced by synthesis and characterization conditions making difficult to perform an adequate comparison with values extracted from simulations. A close inspection of conductivities at a fixed temperature may facilitate a clearer picture of this overall situation. For these purposes, we present the conductivities at room temperature in Figure 11.

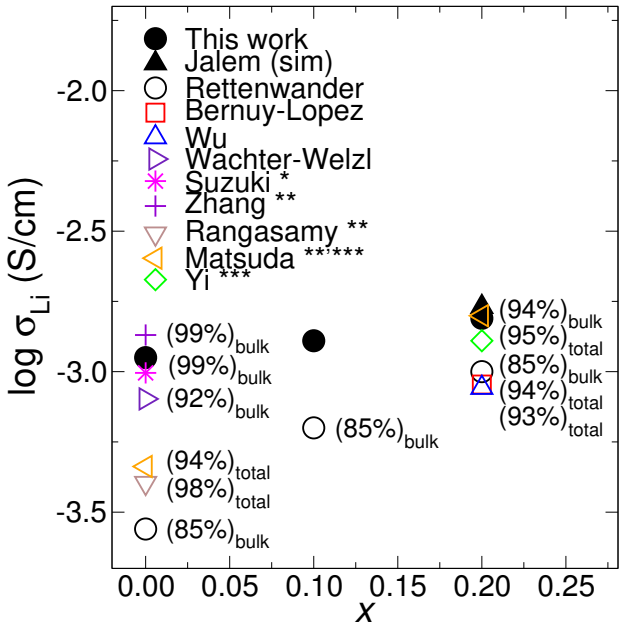

Figure 11: Li-ion bulk and total conductivities at 298 K for $Ga_xAl_{0.2-x}$ at different Ga/Al concentrations. Bulk conductivities calculated from simulations in this work and by Jalem et al.[21] are represented by filled symbols (error bars smaller than symbols). Literature data from experiments by Rettenwander et al.,[11] Bernuy-Lopez et al.,[16] Wu et al.,[49] Wachter-Welzl et al.,[69] Suzuki et al.,[70] Zhang et al.,[61] Rangasamy et al.,[60] Matsuda et al.[59] and Yi et al.[63] are shown for comparison. Relative pellet density, and the nature of sample conductivity (bulk or total) are specified next to each experimental data point; in addition, data for $Ga_{0.0}Al_{0.17}$, $Ga_{0.0}Al_{0.25}$ and $Ga_{0.25}Al_{0.0}$ are identified by (*), (**) and (***) superscripts, respectively.

Figure 11 confirms an increase in conductivity with increasing Ga concentration in $Ga_xAl_{0.2-x}$. Following the discussion in the previous section, this behavior can be explained as follows: at $x = 0$ only Al atoms are substituted on the LLZO Li-ion sites. Non-bonded attractive interactions in the vicinity of Al ions interrupt the diffusion paths of Li ions, limiting the long-range conductivity of the system. As x increases the ratio of Ga to Al ions increases, favoring the association between different diffusion paths as the attractive interatomic interactions originated from Al atoms are progressively diminished. As a consequence, a higher fraction of the Li lattice becomes active in Li diffusion (see Figure 9), resulting in a higher conductivity.

According to our simulations, the bulk conductivity at room temperature of $Ga_{0.0}Al_{0.2}$ is $\sigma_{Ga_{0.0}Al_{0.2}} = 1.1$ mS/cm. There is a significant variation in the values reported in the literature at similar compositions. Wachter-Welzl et al.[69] obtained a maximum conductivity of 0.8 mS/cm from a set of 44 samples, which matches well the one calculated here. In contrast, Rettenwander et al.[11] determined a value of 0.3 mS/cm at 293 K. For $Ga_{0.0}Al_{0.25}$, a number of authors have reported conductivities in the range 0.4-1.3 mS/cm.[59–61]

For the other compositions, our simulations yield $\sigma_{Ga_{0.1}Al_{0.1}} = 1.3$ mS/cm and $\sigma_{Ga_{0.2}Al_{0.0}} = 1.5$ mS/cm at room temperature. $\sigma_{Ga_{0.1}Al_{0.1}}$ is higher than the bulk conductivity from Rettenwander et al.[11] (0.8 mS/cm) for the same composition. However, the difference is smaller compared to that for $Ga_{0.0}Al_{0.2}$. Better agreement is further reached for $Ga_{0.2}Al_{0.0}$, whose conductivity Rettenwander et al. estimates as 1.2 mS/cm. In addition, our results for $Ga_{0.2}Al_{0.0}$ are in good agreement with experimental data reported by Wu et al.[49] (0.8 mS/cm), and Bernuy-Lopez et al.[16] (1.0 mS/cm).

The maximal discrepancy between our estimates and experimentally measured conductivities decreases with increasing content of Ga ions, as shown in Figure 11. One of the major reasons for that is a more pronounced variability in experimental conductivities of Al-substituted LLZO systems in comparison with the full Ga-substituted garnets. In contrast, Ga-substituted LLZO systems exhibit a similar number of bulk[11,59] and total[16,49,63]

conductivities. This may suggest that the various factors involved in the experimental synthesis of single subtituted LLZO may have a lesser impact on samples with a high presence of Ga ions compared with the Al-substituted samples. The sensitivity of conductivity of Al-substituted LLZO to the different experimental conditions has been known previously. For instance, Wachter-Welzl et al.[69] estimated differences up to 2 orders of magnitude for σ_{bulk} for 44 samples of $Ga_{0.0}Al_{0.2}$ sintered at temperatures of 1150 and 1230 °C. Also, the authors reported an inhomogeneous behaviour of conductivity when varying the size of samples, possibly caused by a non-uniform distribution of Al atoms in LLZO. The latter indeed tends to segregate at the GBs[24] making difficult a proper control of the stoichiometry of the substituted garnet.

In general, to validate our theoretical results, accurate experimental measurements of the local Li-ion mobility at the nanoscale on well-defined single crystals are severely needed. In particular, nuclear magnetic resonance (NMR) and neutron total scattering measurements of Al/Ga dual substituted LLZO garnets remain highly desirable. A step in this direction was taken by Rettenwander et al.[13] who used ^{27}Al and ^{71}Ga MAS NMR to determine the substituent site preference and to infer the mean residence time between consecutive Li-ion jumps.

4 Conclusions

In this work, the effects of Al and Ga substitution in LLZO garnets (placed in Li_{T_d} sites) on Li-ion mobility were investigated, providing new insights into the role of each substituent cation in the local Li-ion mobility. In addition to MD, the GSHMC method[18] was employed to simulate $Li_{6.4}Ga_xAl_{0.2-x}La_3Zr_2O_{12}$ (x = 0.0, 0.1, 0.2) for up to 320 ns at temperatures ranging from 193 to 313 K, using a force field specifically optimized for this system. To the best of our knowledge, this is the first time that such a low temperature region is explored in force-field simulations of garnet materials.

Substitution of Li by Ga or Al ions is a well-known method to induce the phase transition from poorly conductive tetragonal LLZO, to highly conductive cubic LLZO at room temperature. We found that when located in the T_{d} sites of the Li lattice, both Ga and Al tend to deactivate Li-ion diffusion within a 4 Å radius (which is the distance to the nearest four T_{d} sites). We put forward that this is not just a consequence of physical blocking, but is possibly due to the stabilizing effect these cations have over the surrounding Li ions. More specifically, the potential energy in the T_{d} sites adjacent to the dopants is lower than that in other T_{d} sites. In fact, the vacancies generated by Al/Ga substitution remained adjacent to the cations, which means they did not contribute in promoting Li hopping. However, while isolated Ga tend to allow diffusion in a limited capacity in their immediate surroundings, the non-bonded attractive interactions associated with Al lead to complete blockage of diffusion in the neighboring Li paths. Moreover, when Al ions were within 8 Å from each other, the synergistic effect can generate large volumes of material where Li-ion diffusion is effectively inexistent. Hence, our work is in line with Travis et al. experimental findings,[56] who found that a maximum Li conductivity in single substituted LLZO is reached at a concentration of 6.5 Li pfu, solely due to complete transition from tetragonal to cubic LLZO. A concentration of dopant that further reduces the amount of Li after the tetragonal to cubic transition will tend to reduce the conductivity.

The difference between the diffusivities of Ga-substituted and Al-substituted LLZO reaches its highest value at the lowest temperature. Indeed, at 233 K, Li ions that visit more than one T_{d} site in Ga-substituted LLZO occupy 37% of the total available volume for diffusion, whereas this value is reduced to 30% in the case of Al-substituted LLZO. As the temperature increases, the rise in kinetic energy of Li ions reduces the effect of attractive interatomic interactions in the nearby regions of Al ions. This reduces the gap in the Li accessible volumes. Thus, at 313 K the effective volumes for diffusion become 45% and 42% for Ga- to Al-substituted LLZO, respectively. As a result, the calculated diffusion of $Ga_{0.2}Al_{0.0}$ is found to be up to 3 and 1.1 times faster than $Ga_{0.0}Al_{0.2}$ at 193K and 313K, respectively.

Our results show that in the bulk region, Li-ion conductivity increases with the Ga content at a constant dopant concentration. Although these observations fit qualitatively to the available experimental data, the quantitative discrepancies are found to increase as the temperature decreases. This can be caused by several factors, including, the relative density and homogeneity of the samples and the synthesis process. Corrections to these effects are beyond the scope of this work since they would imply experimental investigation on local Li-ion dynamics in the bulk (to avoid GB and porosity effects). In addition, a closer inspection of experimental data at 298 K suggests that the conductivity in Ga-substituted LLZO systems is less affected than Al- by differences in the experimental synthesis conditions. In consequence, bigger discrepancies between our prediction and experimental data can be expected for systems with higher content of Al ions. Accurate experimental measurements of local Li-ion diffusion (e.g. using NMR or pair distribution functions obtained with synchrotron or neutron diffraction data) would be of high interest to readily validate the simulations.

Acknowledgement

We acknowledge the financial support by the Ministerio de Economía y Competitividad (MINECO) of the Spanish Government through grants ENE2016-81020-R, MTM2016-76329-R (AEI/FEDER, EU) and BCAM Severo Ochoa accreditation SEV-2017-0718. This work was supported by the BERC 2018-2021 Program and by ELKARTEK Programme, grant KK-2018/00054, funded by the Basque Government.

Supporting Information Available

Potential energy distributions for $Ga_xAl_{0.2-x}$, (x = 0.0, 0.1, 0.2) are shown in section S1. Fine tuning of the interatomic potential is described in section S2. Integrated autocorrelation functions of potential energies estimated during the equilibration phase of MD and GSHMC simulations are listed in section S3. Finally, the thermal expansion for Al/Ga-substituted

LLZO is shown in section S4. This material is available free of charge via the Internet at `http://pubs.acs.org/`.

References

(1) Stramare, S.; Thangadurai, V.; Weppner, W. Lithium Lanthanum Titanates: A Review. *Chem. Mat.* **2003**, *15*, 3974–3990.

(2) Martínez-Juárez, A.; Pecharromán, C.; Iglesias, J.; Rojo, J. Relationship between Activation Energy and Bottleneck Size for Li^+ Ion Conduction in NASICON Materials of Composition LiMM‘(PO4)3; M, M‘ = Ge, Ti, Sn, Hf. *J. Phys. Chem. B* **1998**, *102*, 372–375.

(3) Rodger, A.; Kuwano, J.; West, A. Li^+ Ion Conducting γ Solid Solutions in the Systems Li_4XO_4-Li_3YO_4: X=Si, Ge, Ti; Y=P, As, V; Li_4XO_4-$LiZO_2$: Z=Al, Ga, Cr and Li_4GeO_4-Li_2CaGeO_4. *Solid State Ionics* **1985**, *15*, 185–198.

(4) Thangadurai, V.; Narayanan, S.; Pinzaru, D. Garnet-Type Solid-State Fast Li Ion Conductors for Li Batteries: Critical Review. *Chem. Soc. Rev.* **2014**, *43*, 4714–4727.

(5) Deiseroth, H.-J.; Kong, S.-T.; Eckert, H.; Vannahme, J.; Reiner, C.; Zaiß, T.; Schlosser, M. Li_6PS_5X: A Class of Crystalline Li-Rich Solids With an Unusually High Li^+ Mobility. *Angew. Chem., Int. Ed.* **2008**, *47*, 755–758.

(6) Tatsumisago, M.; Nagao, M.; Hayashi, A. Recent Development of Sulfide Solid Electrolytes and Interfacial Modification for All-Solid-State Rechargeable Lithium Batteries. *J. Asian Ceram. Soc.* **2013**, *1*, 17–25.

(7) Cao, C.; Li, Z.-B.; Wang, X.-L.; Zhao, X.-B.; Han, W.-Q. Recent Advances in Inorganic Solid Electrolytes for Lithium Batteries. *Front. Energy Res.* **2014**, *2*, 25.

(8) Zhu, Y.; He, X.; Mo, Y. Origin of Outstanding Stability in the Lithium Solid Electrolyte Materials: Insights from Thermodynamic Analyses Based on First-Principles Calculations. *ACS Appl. Mater. Interfaces* **2015**, *7*, 23685–23693.

(9) Richards, W.; Miara, L.; Wang, Y.; Kim, J.; Ceder, G. Interface Stability in Solid-State Batteries. *Chem. Mater.* **2016**, *28*, 266–273.

(10) Awaka, J.; Kijima, N.; Hayakawa, H.; Akimoto, J. Synthesis and Structure Analysis of Tetragonal $Li_7La_3Zr_2O_{12}$ with the Garnet-Related Type Structure. *J. Solid State Chem.* **2009**, *182*, 2046–2052.

(11) Rettenwander, D.; Redhammer, G.; Preishuber-Pflügl, F.; Cheng, L.; Miara, L.; Wagner, R.; Welzl, A.; Suard, E.; Doeff, M. M.; Wilkening, M.; Fleig, J.; Amthauer, G. Structural and Electrochemical Consequences of Al and Ga Cosubstitution in $Li_7La_3Zr_2O_{12}$ Solid Electrolytes. *Chem. Mater.* **2016**, *28*, 2384–2392.

(12) Wagner, R.; Redhammer, G.; Rettenwander, D.; Senyshyn, A.; Schmidt, W.; Wilkening, M.; Amthauer, G. Crystal Structure of Garnet-Related Li-Ion Conductor $Li_{7-3x}Ga_xLa_3Zr_2O_{12}$: Fast Li-Ion Conduction Caused by a Different Cubic Modification? *Chem. Mater.* **2016**, *28*, 1861–1871.

(13) Rettenwander, D.; Langer, J.; Schmidt, W.; Arrer, C.; Harris, K. J.; Terskikh, V.; Goward, G. R.; Wilkening, M.; Amthauer, G. Site Occupation of Ga and Al in Stabilized Cubic $Li_{7-3(x+y)}Ga_xAl_yLa_3Zr_2O_{12}$ Garnets As Deduced from ^{27}Al and ^{71}Ga MAS NMR at Ultrahigh Magnetic Fields. *Chem. Mater.* **2015**, *27*, 3135–3142.

(14) Shin, D. O.; Oh, K.; Kim, K. M.; Park, K.-Y.; Lee, B.; Lee, Y.-G.; Kang, K. Synergistic Multi-Doping Effects on the $Li_7La_3Zr_2O_{12}$ Solid Electrolyte for Fast Lithium Ion Conduction. *Sci. Rep.* **2015**, *5*, 18053.

(15) Murugan, R.; Thangadurai, V.; Weppner, W. Fast Lithium Ion Conduction in Garnet-Type $Li_7La_3Zr_2O_{12}$. *Angew. Chem., Int. Ed.* **2007**, *46*, 7778–7781.

(16) Bernuy-Lopez, C.; Manalastas, W.; Lopez del Amo, J. M.; Aguadero, A.; Aguesse, F.; Kilner, J. A. Atmosphere Controlled Processing of Ga-Substituted Garnets for High Li-Ion Conductivity Ceramics. *Chem. Mater.* **2014**, *26*, 3610–3617.

(17) Cheng, L.; Park, J. S.; Hou, H.; Zorba, V.; Chen, G.; Richardson, T.; Cabana, J.; Russo, R.; Doeff, M. Effect of Microstructure and Surface Impurity Segregation on the Electrical and Electrochemical Properties of Dense Al-Substituted $Li_7La_3Zr_2O_{12}$. *J. Mater. Chem. A* **2014**, *2*, 172–181.

(18) Akhmatskaya, E.; Reich, S. GSHMC: An Efficient Method for Molecular Simulation. *J. Comput. Phys.* **2008**, *227*, 4934–4954.

(19) Allen, J.; Wolfenstine, J.; Rangasamy, E.; Sakamoto, J. Effect of Substitution (Ta, Al, Ga) on the Conductivity of $Li_7La_3Zr_2O_{12}$. *J. Power Sources* **2012**, *206*, 315–319.

(20) Rettenwander, D.; Geiger, C. A.; Tribus, M.; Tropper, P.; Amthauer, G. A Synthesis and Crystal Chemical Study of the Fast Ion Conductor $Li_{73x}Ga_xLa_3Zr_2O_{12}$ with $x =$ 0.08 to 0.84. *Inorg. Chem.* **2014**, *53*, 6264–6269.

(21) Jalem, R.; Rushton, M.; Manalastas, W.; Nakayama, M.; Kasuga, T.; Kilner, J. A.; Grimes, R. W. Effects of Gallium Doping in Garnet-Type $Li_7La_3Zr_2O_{12}$ Solid Electrolytes. *Chem. Mater.* **2015**, *27*, 2821–2831.

(22) Buschmann, H.; Dölle, J.; Berendts, S.; Kuhn, A.; Bottke, P.; Wilkening, M.; Heitjans, P.; Senyshyn, A.; Ehrenberg, H.; Lotnyk, A.; Duppel, V.; Kienle, L.; Janek, J. Structure and Dynamics of the Fast Lithium Ion Conductor "$Li_7La_3Zr_2O_{12}$". *Phys. Chem. Chem. Phys.* **2011**, *13*, 19378–19392.

(23) Amores, M.; Ashton, T. E.; Baker, P. J.; Cussen, E. J.; Corr, S. A. Fast Microwave-Assisted Synthesis of Li-Stuffed Garnets and Insights into Li Diffusion from Muon Spin Spectroscopy. *J. Mater. Chem. A* **2016**, *4*, 1729–1736.

(24) Buannic, L.; Orayech, B.; López Del Amo, J.-M.; Carrasco, J.; Katcho, N. A.; Aguesse, F.; Manalastas, W.; Zhang, W.; Kilner, J.; Llordés, A. Dual Substitution Strategy to Enhance Li^+ Ionic Conductivity in $Li_7La_3Zr_2O_{12}$ Solid Electrolyte. *Chem. Mater.* **2017**, *29*, 1769–1778.

(25) Klenk, M.; Lai, W. Local Structure and Dynamics of Lithium Garnet Ionic Conductors: Tetragonal and Cubic $Li_7La_3Zr_2O_7$. *Phys. Chem. Chem. Phys.* **2015**, *17*, 8758–8768.

(26) Klenk, M. J.; Lai, W. Finite-Size Effects on the Molecular Dynamics Simulation of Fast-Ion Conductors: A Case Study of Lithium Garnet Oxide $Li_7La_3Zr_2O_{12}$. *Solid State Ionics* **2016**, *289*, 143 – 149.

(27) Burbano, M.; Carlier, D.; Boucher, F.; Morgan, B. J.; Salanne, M. Sparse Cyclic Excitations Explain the Low Ionic Conductivity of Stoichiometric $Li_7La_3Zr_2O_{12}$. *Phys. Rev. Lett.* **2016**, *116*, 135901.

(28) Pedone, A.; Malavasi, G.; Menziani, M. C.; Cormack, A. N.; Segre, U. A New Self-Consistent Empirical Interatomic Potential Model for Oxides, Silicates, and Silica-Based Glasses. *J. Phys. Chem. B* **2006**, *110*, 11780–11795.

(29) Miara, L. J.; Richards, W. D.; Wang, Y. E.; Ceder, G. First-Principles Studies on Cation Dopants and Electrolyte|Cathode Interphases for Lithium Garnets. *Chem. Mater.* **2015**, *27*, 4040–4047.

(30) Lander, L.; Reynaud, M.; Carrasco, J.; Katcho, N. A.; Bellin, C.; Polian, A.; Baptiste, B.; Rousse, G.; Tarascon, J.-M. Unveiling the Electrochemical Mechanisms of $Li_2Fe(SO_4)_2$ Polymorphs by Neutron Diffraction and Density Functional Theory Calculations. *Phys. Chem. Chem. Phys.* **2016**, *18*, 14509–14519.

(31) Plimpton, S. Fast Parallel Algorithms for Short-Range Molecular Dynamics. *J. Comput. Phys.* **1995**, *117*, 1 – 19.

(32) Escribano, B.; Akhmatskaya, E.; Mujika, J. Combining Stochastic and Deterministic Approaches within High Efficiency Molecular Simulations. *Cent. Eur. J. Math.* **2013**, *11*, 787–799.

(33) Fernández-Pendás, M.; Akhmatskaya, E.; Sanz-Serna, J. Adaptive Multi-Stage Integrators for Optimal Energy Conservation in Molecular Simulations. *J. Comput. Phys.* **2016**, *327*, 434–449.

(34) Pronk, S.; Páll, S.; Schulz, R.; Larsson, P.; Bjelkmar, P.; Apostolov, R.; Shirts, M.; Smith, J.; Kasson, P.; Van Der Spoel, D.; Hess, B.; Lindahl, E. GROMACS 4.5: A High-Throughput and Highly Parallel Open Source Molecular Simulation Toolkit. *Bioinformatics* **2013**, *29*, 845–854.

(35) Duane, S.; Kennedy, A.; Pendleton, B.; Roweth, D. Hybrid Monte Carlo. *Phys. Lett. B* **1987**, *195*, 216–222.

(36) Horowitz, A. A Generalized Guided Monte Carlo Algorithm. *Phys. Lett. B* **1991**, *268*, 247–252.

(37) Akhmatskaya, E.; Fernández-Pendás, M.; Radivojević, T.; Sanz-Serna, J. Adaptive Splitting Integrators for Enhancing Sampling Efficiency of Modified Hamiltonian Monte Carlo Methods in Molecular Simulation. *Langmuir* **2017**, *33*, 11530–11542.

(38) Wee, C.; Sansom, M.; Reich, S.; Akhmatskaya, E. Improved Sampling for Simulations of Interfacial Membrane Proteins: Application of Generalized Shadow Hybrid Monte Carlo to a Peptide Toxin/Bilayer System. *J. Phys. Chem. B* **2008**, *112*, 5710–5717.

(39) Mujika, J.; Escribano, B.; Akhmatskaya, E.; Ugalde, J.; Lopez, X. Molecular Dynamics Simulations of Iron- and Aluminum-Loaded Serum Transferrin: Protonation of Tyr188 is Necessary to Prompt Metal Release. *Biochemistry* **2012**, *51*, 7017–7027.

(40) Escribano, B.; Akhmatskaya, E.; Reich, S.; Azpiroz, J. Multiple-Time-Stepping Generalized Hybrid Monte Carlo Methods. *J. Comput. Phys.* **2015**, *280*, 1–20.

(41) Escribano, B.; Lozano, A.; Radivojević, T.; Fernández-Pendás, M.; Carrasco, J.; Akhmatskaya, E. Enhancing Sampling in Atomistic Simulations of Solid-State Materials for Batteries: A Focus on Olivine $NaFePO_4$. *Theor. Chem. Acc.* **2017**, *136*.

(42) Bonilla, M.; Lozano, A.; Escribano, B.; Carrasco, J.; Akhmatskaya, E. Revealing the Mechanism of Sodium Diffusion in Na_xFePO_4 Using an Improved Force Field. *J. Phys. Chem. C* **2018**, *122*, 8065–8075.

(43) Essmann, U.; Perera, L.; Berkowitz, M.; Darden, T.; Lee, H.; Pedersen, L. A Smooth Particle Mesh Ewald Method. *J. Chem. Phys.* **1995**, *103*, 8577–8593.

(44) Bussi, G.; Donadio, D.; Parrinello, M. Canonical Sampling through Velocity Rescaling. *J. Chem. Phys.* **2007**, *126*.

(45) Andersen, H. Molecular Dynamics Simulations at Constant Pressure and/or Temperature. *J. Chem. Phys.* **1980**, *72*, 2384–2393.

(46) Radivojević, T.; Fernández-Pendás, M.; Sanz-Serna, J. M.; Akhmatskaya, E. Multi-Stage Splitting Integrators for Sampling with Modified Hamiltonian Monte Carlo Methods. *J. Comput. Phys.* **2018**, *373*, 900 – 916.

(47) Hu, Z.; Liu, H.; Ruan, H.; Hu, R.; Su, Y.; Zhang, L. High Li-ion Conductivity of Al-Doped $Li_7La_3Zr_2O_{12}$ Synthesized by Solid-State Reaction. *Ceram. Int.* **2016**, *42*, 12156–12160.

(48) Djenadic, R.; Botros, M.; Benel, C.; Clemens, O.; Indris, S.; Choudhary, A.; Bergfeldt, T.; Hahn, H. Nebulized Spray Pyrolysis of Al-Doped $Li_7La_3Zr_2O_{12}$ Solid Electrolyte for Battery Applications. *Solid State Ionics* **2014**, *263*, 49–56.

(49) Wu, J.-F.; Chen, E.-Y.; Yu, Y.; Liu, L.; Wu, Y.; Pang, W. K.; Peterson, V. K.; Guo, X. Gallium-Doped $Li_7La_3Zr_2O_{12}$ Garnet-Type Electrolytes with High Lithium-Ion Conductivity. *ACS Appl. Mater. Interfaces* **2017**, *9*, 1542–1552.

(50) Klenk, M.; Boeberitz, S.; Dai, J.; Jalarvo, N.; Peterson, V.; Lai, W. Lithium Self-Diffusion in a Model Lithium Garnet Oxide $Li_5La_3Ta_2O_{12}$: A Combined Quasi-Elastic Neutron Scattering and Molecular Dynamics Study. *Solid State Ionics* **2017**, *312*, 1–7.

(51) Stanje, B.; Rettenwander, D.; Breuer, S.; Uitz, M.; Berendts, S.; Lerch, M.; Uecker, R.; Redhammer, G.; Hanzu, I.; Wilkening, M. Solid Electrolytes: Extremely Fast Charge Carriers in Garnet-Type $Li_6La_3ZrTaO_{12}$ Single Crystals. *Ann. Phys.* **2017**, *529*.

(52) Yu, S.; Siegel, D. Grain Boundary Contributions to Li-Ion Transport in the Solid Electrolyte $Li_7La_3Zr_2O_{12}$ (LLZO). *Chem. Mater.* **2017**, *29*, 9639–9647.

(53) Dawson, J.; Canepa, P.; Famprikis, T.; Masquelier, C.; Islam, M. Atomic-Scale Influence of Grain Boundaries on Li-Ion Conduction in Solid Electrolytes for All-Solid-State Batteries. *J. Am. Chem. Soc.* **2018**, *140*, 362–368.

(54) Hayamizu, K.; Seki, S.; Haishi, T. Lithium Ion Micrometer Diffusion in a Garnet-Type Cubic $Li_7La_3Zr_2O_{12}$ (LLZO) Studied Using ^{7}Li NMR Spectroscopy. *J. Chem. Phys.* **2017**, *146*.

(55) Xu, M.; Park, M. S.; Lee, J. M.; Kim, T. Y.; Park, Y. S.; Ma, E. Mechanisms of Li^+ Transport in Garnet-Type Cubic $Li_{3+x}La_3M_2O_{12}$ (M = Te, Nb, Zr). *Phys. Rev. B* **2012**, *85*, 052301.

(56) Travis, T.; Asma, S.; D., J. M.; Ashfia, H.; L., A. J.; Jeff, W.; Jeff, S. A Tale of Two Sites: On Defining the Carrier Concentration in Garnet-Based Ionic Conductors for Advanced Li Batteries. *Adv. Energy Mater.* **2015**, *5*, 1500096.

(57) Shinawi, H. E.; Janek, J. Stabilization of Cubic Lithium-Stuffed Garnets of the Type "$Li_7La_3Zr_2O_{12}$" by Addition of Gallium. *J. of Power Sources* **2013**, *225*, 13 – 19.

(58) van den Broek, J.; Afyon, S.; Rupp, J. Interface-Engineered All-Solid-State Li-Ion Batteries Based on Garnet-Type Fast Li^+ Conductors. *Adv. Energy Mater.* **2016**, *6*, 1600736.

(59) Matsuda, Y.; Sakaida, A.; Sugimoto, K.; Mori, D.; Takeda, Y.; Yamamoto, O.; Imanishi, N. Sintering Behavior and Electrochemical Properties of Garnet-Like Lithium Conductor $Li_{6.25}M_{0.25}La_3Zr_2O_{12}$ (M: Al^{3+} and Ga^{3+}). *Solid State Ionics* **2017**, *311*, 69–74.

(60) Rangasamy, E.; Wolfenstine, J.; Sakamoto, J. The Role of Al and Li Concentration on the Formation of Cubic Garnet Solid Electrolyte of Nominal Composition $Li_7La_3Zr_2O_{12}$. *Solid State Ionics* **2012**, *206*, 28–32.

(61) Zhang, Y.; Chen, F.; Tu, R.; Shen, Q.; Zhang, X.; Zhang, L. Effect of Lithium Ion Concentration on the Microstructure Evolution and Its Association with the Ionic Conductivity of Cubic Garnet-Type Nominal $Li_7Al_{0.25}La_3Zr_2O_{12}$ Solid Electrolytes. *Solid State Ionics* **2016**, *284*, 53–60.

(62) Cheng, L.; Hou, H.; Lux, S.; Kostecki, R.; Davis, R.; Zorba, V.; Mehta, A.; Doeff, M. Enhanced Lithium Ion Transport in Garnet-Type Solid State Electrolytes. *J. Electroceram.* **2017**, *38*, 168–175.

(63) Yi, E.; Wang, W.; Kieffer, J.; Laine, R. Key Parameters Governing the Densification of Cubic-$Li_7La_3Zr_2O_{12}$ Li^+ Conductors. *J. Power Sources* **2017**, *352*, 156–164.

(64) Yang, S.; Kim, M.; Kim, D.; Jung, H.; Ryu, H.; Han, J.; Lee, M.; Kim, H.-S. Ionic Conductivity of Ga-Doped LLZO Prepared Using Couette-Taylor Reactor for All-Solid Lithium Batteries. *J. Ind. Eng. Chem.* **2017**, *56*, 422–427.

(65) Yi, E.; Wang, W.; Kieffer, J.; Laine, R. M. Flame Made Nanoparticles Permit Processing of Dense, Flexible, Li^+ Conducting Ceramic Electrolyte Thin Films of Cubic-$Li_7La_3Zr_2O_{12}$ (c-LLZO). *J. Mater. Chem. A* **2016**, *4*, 12947–12954.

(66) El-Shinawi, H.; Paterson, G. W.; MacLaren, D. A.; Cussen, E. J.; Corr, S. A. Low-Temperature Densification of Al-Doped $Li_7La_3Zr_2O_{12}$: A Reliable and Controllable Synthesis of Fast-Ion Conducting Garnets. *J. Mater. Chem. A* **2017**, *5*, 319–329.

(67) Weller, J. M.; Whetten, J. A.; Chan, C. K. Synthesis of Fine Cubic $Li_7La_3Zr_2O_{12}$ Powders in Molten LiCl-KCl Eutectic and Facile Densification by Reversal of Li^+/H^+ Exchange. *ACS Appl. Energy Mater.* **2018**, *1*, 552–560.

(68) Yunsung, K.; Hyungyung, J.; L., A. J.; Heeman, C.; Jeff, W.; Jeff, S. The Effect of Relative Density on the Mechanical Properties of Hot-Pressed Cubic $Li_7La_3Zr_2O_{12}$. *J. Am. Ceram. Soc.* **2016**, *99*, 1367–1374.

(69) Wachter-Welzl, A.; Kirowitz, J.; Wagner, R.; Smetaczek, S.; Brunauer, G.; Bonta, M.; Rettenwander, D.; Taibl, S.; Limbeck, A.; Amthauer, G.; Fleig, J. The Origin of Conductivity Variations in Al-Stabilized $Li_7La_3Zr_2O_{12}$ Ceramics. *Solid State Ionics* **2018**, *319*, 203–208.

(70) Suzuki, Y.; Kami, K.; Watanabe, K.; Watanabe, A.; Saito, N.; Ohnishi, T.; Takada, K.; Sudo, R.; Imanishi, N. Transparent Cubic Garnet-Type Solid Electrolyte of Al_2O_3-Doped $Li_7La_3Zr_2O_{12}$. *Solid State Ionics* **2015**, *278*, 172–176.

Graphical TOC Entry